# The Role of Clouds in Modulating Global Aerosol Direct Radiative Effects in Spaceborne Active Observations and the Community Earth System Model

ALEXANDER V. MATUS AND TRISTAN S. L'ECUYER

*University of Wisconsin–Madison, Madison, Wisconsin*

JENNIFER E. KAY

*University of Colorado Boulder, Boulder, Colorado*

CECILE HANNAY AND JEAN-FRANCOIS LAMARQUE

*National Center for Atmospheric Research,* Boulder, Colorado*

(Manuscript received 16 June 2014, in final form 13 January 2015)

ABSTRACT

Observational benchmarks of global and regional aerosol direct radiative effects, over all surfaces and all sky conditions, are generated using *CloudSat*'s new multisensor radiative fluxes and heating rates product. Improving upon previous techniques, the approach leverages the capability of *CloudSat* and *CALIPSO* to retrieve vertically resolved estimates of cloud and aerosol properties required for complete and accurate assessment of aerosol direct effects under all conditions. The global annually averaged aerosol direct radiative effect is estimated to be $-1.9\,\mathrm{W\,m^{-2}}$ with an uncertainty range of $\pm 0.6\,\mathrm{W\,m^{-2}}$, which is in better agreement with previously published estimates from global models than previous satellite-based estimates. Detailed comparisons against a fully coupled simulation of the Community Earth System Model, however, reveal that this agreement on the global annual mean masks large regional discrepancies between modeled and observed estimates of aerosol direct effects. A series of regional analyses demonstrate that, in addition to previously documented biases in simulated aerosol distributions, the magnitude and sign of these discrepancies are often related to model biases in the geographic and seasonal distribution of clouds. A low bias in stratocumulus cloud cover over the southeastern Pacific, for example, leads to an overestimate of the radiative effects of marine aerosols in the region. Likewise, errors in the seasonal cycle of low clouds in the southeastern Atlantic distort the radiative effects of biomass burning aerosols from southern Africa. These findings indicate that accurate assessment of aerosol direct effects requires models to correctly represent not only the source, strength, and optical properties of aerosols, but their relative proximity to clouds as well.

## 1. Introduction

Aerosols directly alter radiative flux exchanges between the surface and the top of the atmosphere (TOA) by scattering and absorbing shortwave radiation (Yu et al. 2006). Known as aerosol direct radiative effects (DRE), these interactions play a significant yet still uncertain role in climate. Large uncertainties in global estimates of DRE currently exist as a result of incomplete knowledge of aerosol and environmental characteristics (Anderson et al. 2005; Jaeglé et al. 2011; Satheesh and Krishna Moorthy 2005). Reducing these uncertainties requires improved understanding of aerosol optical properties (e.g., aerosol optical depth, asymmetry parameter, and single scattering albedo) and the albedo of the underlying surface (Hansen et al. 1997; Myhre et al. 2005).

While aerosol DRE may be evaluated at any level of the atmosphere, the two most important levels to consider from a radiative balance perspective are the TOA and surface. Aerosol direct effects at the TOA represent the overall impact of aerosols on global radiative balance,

* The National Center for Atmospheric Research is sponsored by the National Science Foundation.

*Corresponding author address:* Alexander V. Matus, University of Wisconsin–Madison, 1225 W. Dayton St., Madison, WI 53715.
E-mail: amatus@wisc.edu

DOI: 10.1175/JCLI-D-14-00426.1

whereas surface direct radiative effects govern the partitioning of these impacts between the atmosphere and ocean. The latter has important implications for the role of aerosols in the climate system since the atmosphere and ocean respond to external forcings on very different time scales. At the TOA, scattering aerosols typically exert a negative DRE, while absorbing aerosols produce a negative DRE over dark surfaces (e.g., ocean) and a positive DRE over bright surfaces (e.g., sea ice and desert) or bright clouds. A positive DRE at the TOA represents an addition of energy to the Earth–atmosphere system (a net warming effect) whereas a negative DRE denotes a loss of energy (a net cooling effect) (Yu et al. 2006). Since both absorbing and scattering aerosols reduce the energy incident at the surface, aerosol DRE at the surface is always negative.

Global climate models, while providing useful benchmarks for global estimates of DRE, have been shown to exhibit deficiencies in their ability to correctly represent the optical properties and relative positions of clouds and aerosols (Schulz et al. 2006; Kay et al. 2012). Quijano et al. (2000) and Penner (2003), for example, demonstrate that models must correctly place overlapping cloud and aerosol layers in the vertical to accurately compute radiative fluxes. Likewise, Chung et al. (2005) show that uncertainty in the modeled direct radiative forcing of anthropogenic aerosols ranges sixfold (from $-0.1$ to $-0.6\,\mathrm{W\,m^{-2}}$) depending on the relative vertical distributions of aerosols and clouds. Improving the model representation of aerosol radiative effects in cloudy regions is therefore critical for improving global assessments of aerosol climate forcing. It follows that high-quality observations of the relative placement of aerosols and clouds are necessary for validating and effectively constraining climate model simulations of aerosol radiative effects (Chin et al. 2009).

As satellite remote sensing remains the only means of observing the large spatial and temporal variability in aerosol properties, satellite observations have been used extensively to perform global estimates of DRE (Chin et al. 2009; Yu et al. 2006; Bergamo et al. 2008; Di Biagio et al. 2010). However, the passive sensors that lie at the root of many previous studies measure column-averaged properties and have limited capabilities to resolve the vertical distributions of clouds and aerosols. Retrievals of aerosol properties from passive sensors are often impossible or highly biased in the presence of clouds and over bright surfaces, which severely limits our ability to quantify DRE in cloudy skies or over many land areas (Remer et al. 2005; Kaufman et al. 2005). With coverage limited to cloud-free oceans, passive satellite-based estimates of DRE range from $-4$ to $-6\,\mathrm{W\,m^{-2}}$ (Bellouin et al. 2005; Loeb and Manalo-Smith 2005; Yu et al. 2006; Myhre et al. 2007).

Satellite remote sensing of aerosols over cloud and land surfaces, while previously elusive, is now possible using a combination of active and passive sensors (Torres et al. 2007; Omar et al. 2009; de Graaf et al. 2012; Waquet et al. 2009; Patadia et al. 2008). These new measurements are critical since clouds modify the radiative effects of aerosols by altering the underlying surface albedo (Haywood 2003; Myhre et al. 2005). While aerosols typically exert a negative DRE, absorbing aerosols residing over a bright cloud can produce a positive DRE (Chand et al. 2009; Wilcox 2012). The strength of the warming effect from absorbing aerosols is highly sensitive to the reflectance and coverage of any underlying clouds, highlighting the need for collocated cloud and aerosol measurements (Winker et al. 2010).

This study seeks to overcome previous observational limitations using new multisensor aerosol, cloud, and radiative flux products from the A-Train satellite constellation (L'Ecuyer and Jiang 2010). The dataset features collocated observations from *CloudSat*, *CALIPSO*, MODIS, and AMSR-E sensors, specifically designed to identify the precise location of clouds and aerosols and provide vertically resolved estimates of water contents, cloud particle size, and aerosol optical depth (AOD). This combination of active and passive observations provides the unique opportunity to estimate aerosol radiative effects in historically poorly sampled regimes including those above clouds and over land surfaces. The unprecedented ability of these sensors to resolve the vertical structure of clouds and aerosols thus offers unique insights into the complex role clouds play in modulating aerosol direct effects.

Given recent advances in satellite remote sensing of clouds and aerosols, it is necessary to revisit global assessments of aerosol direct effects. This work is motivated by two expected outcomes. First, the combination of active and passive observations will provide a more complete estimate of global DRE than conventional estimates based exclusively from passive observations. Second, biases in modeled DRE will be largest over regions where cloud fields are poorly simulated (e.g., stratocumulus over the southeastern Pacific). Given that clouds have been shown to exert significant influence on aerosol direct effects, biases in modeled DRE may be larger over regions where cloud cover is poorly simulated in models. Such errors, in turn, have potentially strong implications for the ability of models to simulate anthropogenic aerosol radiative forcing. If clouds impact the radiative effects of all aerosols, then it follows that clouds also impact the radiative forcing of anthropogenic aerosols.

Here we present new estimates of the global distribution of aerosol direct effects, in both clear and cloudy skies, using a novel approach that leverages the strengths

of *CloudSat* and *CALIPSO*. These new estimates are used to evaluate the simulated representation of aerosol direct effects in the Community Earth System Model (CESM). While the modeled estimate of global, annually averaged DRE agrees well with the new observational estimate, large regional biases exist. These biases likely result from a combination of errors in aerosol sources, aerosol optical properties, and cloud cover. Assessing the model representation of aerosols has been discussed in greater detail elsewhere (Lamarque et al. 2013; Liu et al. 2012; Neale and Chen 2010). Here, the new capability of A-Train sensors to estimate aerosol radiative effects over all surfaces and in all sky conditions will be used to assess the contribution of cloud cover biases to errors in CESM-simulated aerosol radiative effects.

## 2. Datasets

### a. CloudSat's 2B-FLXHR-lidar data product

*CloudSat*'s level 2B radiative fluxes and heating rates with lidar (2B-FLXHR-lidar) data product provides observationally constrained radiative transfer calculations of broadband radiative fluxes and heating rates (Henderson et al. 2013). Vertical distributions of liquid and ice cloud effective radii and water contents from *CloudSat*'s level 2B cloud water content product (2B-CWC) are combined with temperature and humidity profiles from the European Centre for Medium-Range Weather Forecasts (ECMWF) analyses as well as surface albedo and emissivity data from the International Geosphere–Biosphere Programme (IGBP) global land surface classification. Collectively, these data initialize a broadband radiative flux model, known as BUGSrad, to compute vertical profiles of radiative fluxes and heating rates.

BUGSrad is a two-stream, adding-doubling solution to the radiative transfer equation introduced by Ritter and Geleyn (1992). The model assumes a plane-parallel atmosphere over the 1.4 km × 1.8 km *CloudSat* field of view. Molecular absorption and scattering is computed using the correlated-$k$ method of Fu and Liou (1992). The delta-Eddington approximation is applied over six shortwave bands and a constant-hemisphere approximation is applied over 12 longwave bands. The bands are then weighted and combined into broadband estimates of shortwave and longwave fluxes. Finally, the algorithm computes the pressure derivative of net radiative flux to derive vertical atmospheric heating rates:

$$\mathcal{H} = \frac{g}{C_p}\frac{\partial F^{\text{net}}}{\partial p}. \quad (1)$$

The resulting fluxes and heating rates are output for each *CloudSat* footprint at a vertical resolution of 240 m, forming the standard *CloudSat* radar-only 2B-FLXHR data product (L'Ecuyer et al. 2008). The 2B-FLXHR-lidar data product used in this study builds on the basic 2B-FLXHR framework to include several refinements that are particularly relevant for evaluating aerosol direct effects (Henderson et al. 2013). By including coincident lidar observations from *CALIPSO* and radiance measurements from MODIS, the representation of thin cirrus, marine stratocumulus, and aerosols have all been improved in the radiative flux calculations.

TABLE 1. Optical properties of the six *CALIPSO* aerosol types in the visible band, including radii for both fine and coarse modes, single scattering albedo, and asymmetry parameter.

| Aerosol type | $r$ | | $\omega$ | $g$ |
|---|---|---|---|---|
| | Fine | Coarse | | |
| Marine | — | 1.22 | 0.99 | 0.54 |
| Dust | 0.2 | 2.84 | 0.99 | 0.76 |
| Polluted continental | 0.14 | 3.55 | 0.96 | 0.35 |
| Clean continental | — | 2.63 | 1.00 | 0.74 |
| Polluted dust | 0.21 | 3.16 | 0.96 | 0.39 |
| Smoke | 0.14 | 3.73 | 0.44 | 0.14 |

Radiative flux calculations are further constrained using vertically resolved satellite observations of cloud, precipitation, and aerosol properties. Cloud location in 2B-FLXHR-lidar is determined based on *CloudSat*'s level 2B geometrical profiling with lidar product (2B-GEOPROF-lidar) and cloud properties are assigned based on a combination of *CloudSat*'s radar-only 2B-CWC product (2B-CWC-RO), the MODIS-based level 2B cloud optical depth product (2B-TAU), and *CALIPSO*'s version 3 products. Precipitation location and intensity are identified using *CloudSat*'s level 2C precipitation column algorithm (2C-PRECIP-COLUMN) product, which retrieves cloud and rain liquid water contents and estimates the vertical extent of liquid precipitation in the column. *CALIPSO* lidar backscatter retrievals supply the aerosol information used in the 2B-FLXHR-lidar data product. The location and optical depth of aerosols are obtained from *CALIPSO*'s 5-km aerosol layer product, while aerosol types and vertical distribution are retrieved using *CALIPSO*'s vertical feature mask product (Vaughan et al. 2009).

Aerosols are classified by type using the *CALIPSO* aerosol models, based on a cluster analysis of AERONET measurements as described in Omar et al. (2009). Each aerosol layer is assigned a value of single scattering albedo and asymmetry parameter based on the *CALIPSO* 532-nm aerosol optical depth and mean radius, using a technique similar to that employed in the Spectral Radiation-Transport Model for Aerosol Species (SPRINTARS) global transport model (Takemura et al. 2002). Table 1 summarizes the mean optical properties of the six *CALIPSO* aerosol types in the

visible band, including the effective radii of fine and coarse modes, single scattering albedo, and asymmetry parameter.

Given that radiative fluxes are calculated using a radiative transfer model, aerosol-free conditions can be readily simulated by simply setting all aerosol fields to zero. The algorithm performs two independent sets of flux calculations—one with aerosol included and another with aerosol artificially removed—so that DRE may be computed as the difference in net radiative flux (downwelling minus upwelling) between the two sets of outputs:

$$\mathrm{DRE} = (F^{\downarrow} - F^{\uparrow})_{\mathrm{aero}} - (F^{\downarrow} - F^{\uparrow})_{\mathrm{noaero}}. \qquad (2)$$

This satellite-based approach to quantify aerosol DRE mimics that adapted to compute DRE from climate model simulations, thus providing a more direct means for comparing against model output. As previously mentioned, this study only considers the shortwave DRE at the top of the atmosphere. To account for the diurnal cycle of solar insolation, the radiative transfer calculations simulate all possible zenith angles in 2-h increments. The average of the resulting fluxes approximates the diurnal mean but does not account for diurnal variations in cloud cover. Although release 4 of the 2B-FLXHR-lidar dataset uses temperature and humidity from ECMWF analyses, it should be noted that the source of temperature and humidity information has a negligible effect on the estimates of aerosol DRE analyzed here since they derive from flux differences.

### b. Uncertainties

Any uncertainties in *CALIPSO* aerosol retrievals will ultimately influence the 2B-FLXHR-lidar estimates of aerosol radiative effects. It is important to note, however, that these uncertainties are likely much smaller than those encountered in individual scenes or limited field experiments resulting from significant reduction of random errors over the large space and time scales analyzed. The global median relative difference between AERONET and *CALIPSO* AOD, for example, is 25% for AOD greater than 0.1, with differences possibly resulting from cloud contamination, scene inhomogeneity, instrument view angle differences, *CALIPSO* retrieval errors, and detection limits (Omar et al. 2013). Additional validation studies have revealed a low bias in *CALIPSO* estimates of AOD with respect to other global measurements and retrievals (Redemann et al. 2012; Schuster et al. 2012). Recent studies have also shown that *CALIPSO* may suffer from uncertainty in the classification of aerosol types (Omar et al. 2013), can misclassify dense aerosol layers as clouds (Schuster et al. 2012), and may fail to detect aerosols with low AOD, especially in the presence of clouds (Kacenelenbogen et al. 2014).

To assess the uncertainty in simulated fluxes due to errors in *CALIPSO* aerosol products, Henderson et al. (2013) conducted several sensitivity studies where 1) *CALIPSO* AOD retrievals were increased and decreased by a factor of 2, a conservative approximation to the error estimates of Kittaka et al. (2011), 2) all nonmarine aerosols were changed to smoke, 3) all nonmarine aerosols were changed to dust, and 4) all smoke aerosols were changed to dust. Given that the goal here is not to perfectly represent small spatial and temporal variations in aerosol properties but rather to assume characteristics that are reasonably representative of large-scale mean conditions, the variance between these five cases provides conservative bounds on the potential error in simulated fluxes resulting from both retrieval errors and errors in assumed single scattering properties. All uncertainties reported on the subsequent figures derive from the standard deviation of these individual assessments (five perturbed estimates and the original unperturbed estimate), assuming that the error sources are independent and uncorrelated.

### c. Community Earth System Model

CESM is a fully coupled global climate model that provides state-of-the-art representations of Earth's past, present, and future climate. The model architecture consists of five geophysical component models that simultaneously simulate Earth's atmosphere, ocean, land surface, sea ice, and land ice (Hurrell et al. 2013). All five models communicate using a central coupler component within a fully coupled model environment. Physical atmospheric processes are represented using version 5.1 of the Community Atmosphere Model (CAM5), which offers several improvements over its predecessor, CAM4, including an enhanced treatment of stratus–radiation–turbulence interactions, shallow convection, and stratiform microphysics (Neale and Chen 2010). In CESM1(CAM5), aerosols may exist attached to hydrometeors or as interstitial particles (suspended in clear or cloudy air) that can be transported in three dimensions. The CAM5 simulation invokes the three-mode prognostic Modal Aerosol Model (MAM) scheme (Liu et al. 2012) and the Rapid Radiative Transfer Model for GCMs (RRTMG) radiation scheme, which features a distinct set of aerosol and aerosol-free radiation calculations similar to those employed in the 2B-FLXHR-lidar algorithm (Worley and Craig 2012).

The present study analyzes model output from a fully coupled CESM1(CAM5) ensemble member (denoted as b.e10.B20TRC5CN.f09_g16.001) simulated at 1° spatial resolution. Simulated estimates of monthly-mean DRE

TABLE 2. Global estimates of annual-mean DRE ($W\,m^{-2}$) from FLXHR-lidar and CESM1(CAM5) datasets. The fractional occurrence for each category is shown in parentheses.

| Dataset | Surface | Clear sky | Cloudy sky | | All sky |
|---|---|---|---|---|---|
| | | | Thin ($\tau < 1$) | Thick ($\tau > 1$) | |
| FLXHR-lidar | Land + sea ice | −2.2 (14) | −1.6 (12) | +0.8 (17) | −1.5 (44) |
| | Ocean | −2.6 (16) | −2.2 (13) | −0.3 (27) | −2.0 (56) |
| | Global | −2.6 (31) | −2.0 (25) | +0.1 (44) | −1.9 (100) |
| CESM1(CAM5) | Land + sea ice | −2.0 (15) | +0.8 (29) | | −0.4 (44) |
| | Ocean | −3.9 (21) | −1.2 (35) | | −2.1 (56) |
| | Global | −3.4 (36) | −0.6 (64) | | −1.7 (100) |

are analyzed over the time period of 2000–05, which represents a subset of the full simulation that runs from 1850 to 2005. Although the specific time periods differ between the model and observations, this difference has a limited effect on the results since interannual variability in DRE is sufficiently small (less than $\pm 0.03\,W\,m^{-2}$ between both datasets) compared to discrepancies between observed and simulated DRE.

### d. Methodology

The FLXHR-lidar dataset comprises $285 \times 10^6$ radiative flux profiles with near-global coverage (82.5°S–82.5°N) from July 2006 to April 2011. For quality control, profiles with incomplete or missing input data are removed from the dataset. Data are screened based on the quality control flags included in the dataset that test for the following criteria: high uncertainty or missing cloud water content (CWC), missing 2B-TAU data, missing CALIOP, missing MODIS data mapped to *CloudSat* profiles (MODIS-AUX), missing AMSR-E data mapped to *CloudSat* profiles (AMSR-AUX), or out-of-bounds flux observations. The specific criteria are described in greater detail in Table 14 of the *CloudSat* FLXHR-lidar data product documentation (Henderson and L'Ecuyer 2011).

FLXHR-lidar estimates of DRE are partitioned by surface type and sky conditions to gain insight into the environmental factors that influence aerosol direct effects. Since bright surfaces enhance atmospheric warming from absorbing aerosols while dark surfaces enhance cooling from scattering aerosols, accurate assessment of aerosol direct effects requires knowledge of the underlying surface reflectance. The FLXHR-lidar algorithm accounts for land and ocean reflectance characteristics using surface albedo and emissivity data from the IGBP global surface classification. The IGBP global land cover classification is derived from a suite of observational MODIS products aboard the *Terra* and *Aqua* platforms. Land cover data are gridded at 2.5° spatial resolution to produce high-quality seasonal and annual global composites of 17 land cover types (Moody et al. 2005). The surface of each FLXHR-lidar footprint is categorized as land or ocean. Since the shortwave albedo of sea ice is more representative of land rather than ocean, we group all pixels detecting land or sea ice in one category. Based on this classification, Earth's surface is 56% open ocean and 44% nonocean (i.e., land or sea ice) averaged globally.

Cloud phase, water content, and relative location to aerosol layers also exert influence on the radiative effects exerted by aerosols. Like a bright land surface, clouds may enhance atmospheric heating from absorbing aerosols or mask the cooling imposed by scattering aerosols (Chand et al. 2012; Soden et al. 2004). In this study, sky conditions are categorized as clear sky or cloudy sky. Clear-sky conditions are assessed if neither *CloudSat* nor *CALIPSO* detects cloud or precipitation. If either *CloudSat* or *CALIPSO* detects cloud, however, the profile is labeled as cloudy sky. Based on column-integrated cloud optical depth derived from combined *CloudSat* and *CALIPSO* observations, cloudy-sky pixels are further classified as thin clouds ($\tau < 1$) or thick clouds ($\tau > 1$). The threshold choice of $\tau = 1$ is arbitrarily chosen to separate optically thin cirrus from thicker convective anvils and liquid or mixed-phase clouds. Since thin clouds are more transparent to visible radiation, aerosol direct effects are often comparable to clear-sky conditions when thin cirrus is present.

## 3. Global aerosol direct effects

Table 2 summarizes estimates of annual-mean DRE from the FLXHR-lidar and CESM1(CAM5) datasets as partitioned by surface (land, ocean, and global) and sky conditions (clear sky, cloudy sky with thin clouds, cloudy sky with thick clouds, and all sky). Note that since both model-based and observation-based estimates of DRE derive from independent calculations with aerosol removed, the all-sky DRE can be reconstructed after this separation as the linear sum of the cloudy-sky DRE weighted by the cloud fraction and the clear-sky DRE weighted by the fraction of clear sky:

$$\mathrm{DRE} = \mathrm{DRE}_{\mathrm{cld}} \times \mathrm{CF} + \mathrm{DRE}_{\mathrm{clr}} \times (1 - \mathrm{CF}). \quad (3)$$

The global estimate of all-sky DRE from FLXHR-lidar observations is $-1.9\,\mathrm{W\,m^{-2}}$ with an uncertainty range of $\pm 0.6\,\mathrm{W\,m^{-2}}$. The observed all-sky DRE is 33% stronger over ocean ($-2.0\,\mathrm{W\,m^{-2}}$) than over land ($-1.5\,\mathrm{W\,m^{-2}}$). Since open ocean comprises 56% of all observations, the global estimate is weighted toward the ocean value. Interestingly, the annual-mean DRE in clear skies is comparable over land and ocean despite significantly greater aerosol emissions from terrestrial sources. This suggests that the reduced contrast between aerosols and the higher albedo of land surfaces offsets the larger aerosol concentrations characteristic of continental regions (Myhre 2009). Over regions where thin cloud is detected, the observed estimate of global DRE is $-2.0\,\mathrm{W\,m^{-2}}$. Thin clouds thus weaken the global cooling effect of aerosols by 30%, on average, compared to clear-sky observations. The annual-mean DRE where thick cloud is detected is $+0.1\,\mathrm{W\,m^{-2}}$; however, aerosols over thick clouds exert a warming effect over land ($+0.8\,\mathrm{W\,m^{-2}}$), which offsets a cooling effect over ocean ($-0.3\,\mathrm{W\,m^{-2}}$).

There is good agreement between global estimates of all-sky DRE from FLXHR-lidar observations ($-1.9\,\mathrm{W\,m^{-2}}$) and the CESM1(CAM5) simulation ($-1.7\,\mathrm{W\,m^{-2}}$). Despite this agreement under global all-sky conditions, there are large discrepancies in the estimates of aerosol direct effects over certain surface types and sky conditions. Over land, the observed all-sky DRE is over 3 times stronger than the CESM-simulated DRE. This inconsistency in aerosol DRE over land is most pronounced in cloudy skies, because of an enhanced warming effect simulated in CESM as compared to FLXHR-lidar observations. This enhanced warming effect, which will be discussed in greater detail later in this section, largely offsets any cooling effect and results in a weaker modeled DRE over land.

Over oceans, however, all-sky DRE estimates from CESM agree well with observations owing to compensating high and low biases in clear and cloudy skies, respectively. These differences are indicative of two important sources of uncertainty that will be illustrated more clearly in the regional analyses that follow. First, there are significant differences in the modeled and observed cloud cover, with CESM indicating 38% of all oceanic scenes being clear as compared to only 29% in the observations. Second, there are significant differences between modeled and observed estimates of clear-sky and cloudy-sky DRE that may suggest uncertainties in aerosol amount, optical properties, or sampling biases introduced by differences in the specific scenes that contribute to cloudy-sky and clear-sky calculations. For example, since clear-sky DRE estimates are very sensitive to the solar zenith angle and aerosol optical properties, systematic biases in the frequency with which darker surfaces (e.g., tropical ocean) or scenes with higher aerosol loading enter the clear-sky calculations in CESM may cause systematic overestimates of clear-sky DRE relative to the observations, even if the aerosol properties are correctly prescribed in the model.

Global estimates of clear-sky DRE from FLXHR-lidar and CESM1(CAM5) datasets agree within 30%. However, the observed cloudy-sky DRE ($-1.4\,\mathrm{W\,m^{-2}}$) is more than twice as strong as the simulated cloudy-sky DRE ($-0.6\,\mathrm{W\,m^{-2}}$). For estimates of cloudy-sky DRE, the magnitude of the radiative effect is influenced by the optical thickness of the cloud. Once observations are partitioned by cloud optical depth, it is evident that modeled cloudy-sky DRE agrees better with observed DRE in the presence of optically thick clouds. In particular, CESM-simulated cloudy-sky DRE over land is nearly equivalent to the observational estimate in the presence of thick clouds ($+0.8\,\mathrm{W\,m^{-2}}$). Optically thin clouds, on the contrary, produce estimates of DRE that are in better agreement with clear-sky values.

This result is supported by Fig. 1, which maps the spatial distribution of annual-mean DRE observed in the FLXHR-lidar dataset. Consistent with Table 2, aerosol direct effects are separated by sky conditions, including clear sky, cloudy sky (all clouds), cloudy sky (thin clouds), and cloudy sky (thick clouds). Although FLXHR-lidar observations and CESM1(CAM5) simulations compare favorably for estimates of all-sky DRE, their clear-sky and cloudy-sky DRE estimates disagree. Observed clear-sky DRE, shown in Fig. 1a, is strongest over the North Atlantic and Southeast Asia with values exceeding $-10\,\mathrm{W\,m^{-2}}$ in some locations. Although aerosols exert a warming effect regionally over the bright Sahara, a cooling effect predominates globally as evidenced by the negative global estimate of clear-sky DRE ($-2.6\,\mathrm{W\,m^{-2}}$). The uncertainty of the clear-sky DRE estimate is $\pm 0.6\,\mathrm{W\,m^{-2}}$, which is lower than in cloudy skies. The global pattern of DRE with optically thin clouds is similar to that with clear skies, as shown in Figs. 1a and 1c. Since thin clouds are nearly transparent to shortwave radiation, shortwave aerosol direct effects are not significantly altered compared to clear-sky conditions.

Figure 1d reveals a considerably different pattern for aerosol direct effects in the presence of optically thick clouds ($\tau > 1$). Under these conditions, the global estimate of DRE is $+0.1\,\mathrm{W\,m^{-2}}$ with an uncertainty range of $\pm 1.0\,\mathrm{W\,m^{-2}}$. Positive aerosol direct effects are observed over known source regions of absorbing dust aerosols (e.g., northern Africa and western Australia) and absorbing smoke aerosols (e.g., southern Africa and

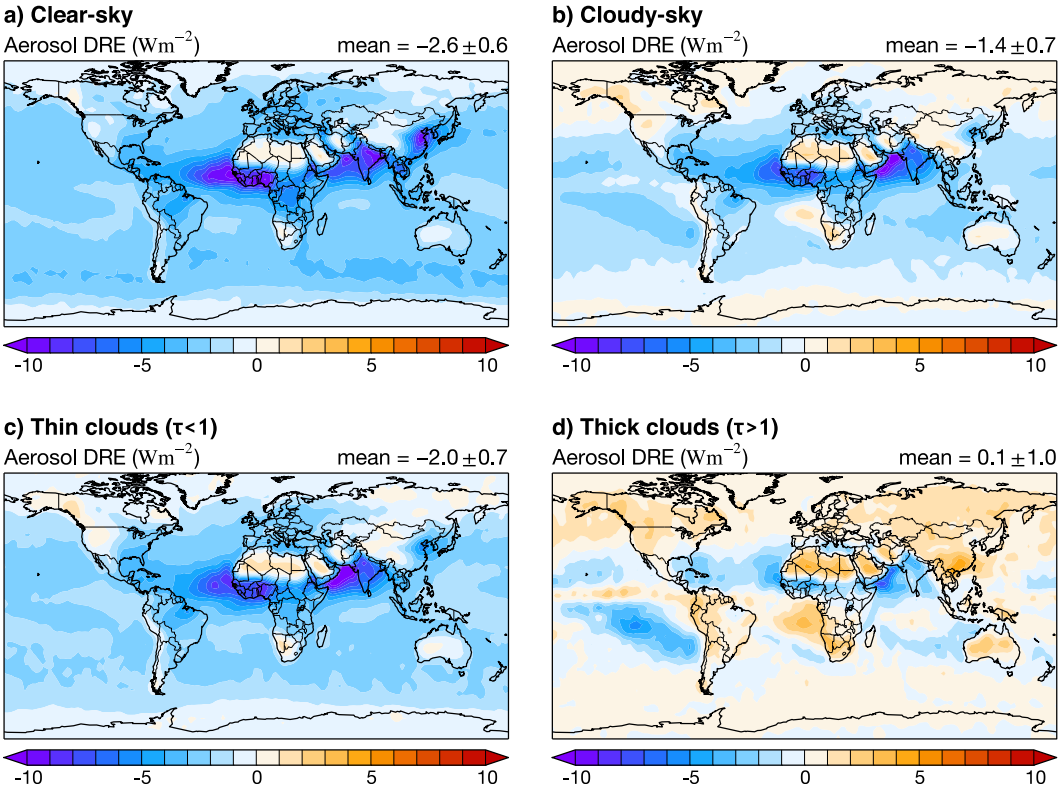


FIG. 1. Annual-mean DRE observed from the FLXHR-lidar dataset, as partitioned by sky conditions. Estimates of the global mean and uncertainty are displayed in the top-right corner of each panel.

Southeast Asia), where the magnitude of cloudy-sky DRE exceeds $+2\,\mathrm{W\,m^{-2}}$. Although absorbing aerosols residing over optically thick clouds may exert a net warming effect, it is also possible for above-cloud aerosols to exert a net cooling effect. If the aerosol optical depth is comparable in magnitude to the cloud optical depth, nonabsorbing aerosols may enhance the reflection of shortwave radiation. Negative aerosol direct effects are observed over the northeastern Atlantic, southeastern Pacific, and Arabian Sea where relatively high AOD is detected by *CALIPSO* observations (see Fig. 2). However, it is worth noting that large uncertainties may exist with DRE observations around cloud edges because of the possible misclassification of dust aerosol as cloud (Omar et al. 2009). Finally, Fig. 1b shows the global pattern of DRE in the presence of all clouds. Collectively, the maps from Fig. 1 highlight that aerosol direct effects are spatially heterogeneous and highly sensitive to cloud cover.

Global maps of all-sky DRE and total cloud fraction from FLXHR-lidar and CESM1(CAM5) datasets are compared in Fig. 3. For consistency with the observationally derived cloud fraction estimates from *CloudSat* and *CALIPSO*, CESM-simulated cloud fraction is evaluated using the GCM-Oriented *CALIPSO* Cloud Product (GOCCP) that simulates what these satellites would observe if flying above an atmosphere similar to that predicted by the model (Chepfer et al. 2010). Both datasets are qualitatively consistent in their representation of aerosol direct effects on a global scale. In both observations and simulations, aerosols exert a cooling effect over dark ocean and a warming effect over bright deserts. The radiative effects of aerosols tend to be strongest near the equator as a result of higher solar insolation. On local scales, however, both the magnitude and pattern of modeled and observed aerosol direct effects are inconsistent. While FLXHR-lidar observes the strongest annual-mean DRE over ocean, CESM1(CAM5) simulates the strongest effects over land. In particular, CESM1(CAM5) significantly overestimates annual-mean DRE over northern Africa and underestimates annual-mean DRE over southern Africa, which is likely due to a combination of errors in the strength of aerosol sources and optical properties over the region. This result is consistent with findings from Shindell et al. (2013), who found that models from phase 5 of CMIP (CMIP5), including CESM1(CAM5), underestimate biomass burning emissions and overestimate absorbing AOD over the Sahara. Despite uncertainties in the aerosol optical properties and optical depth assigned to the satellite observations, even

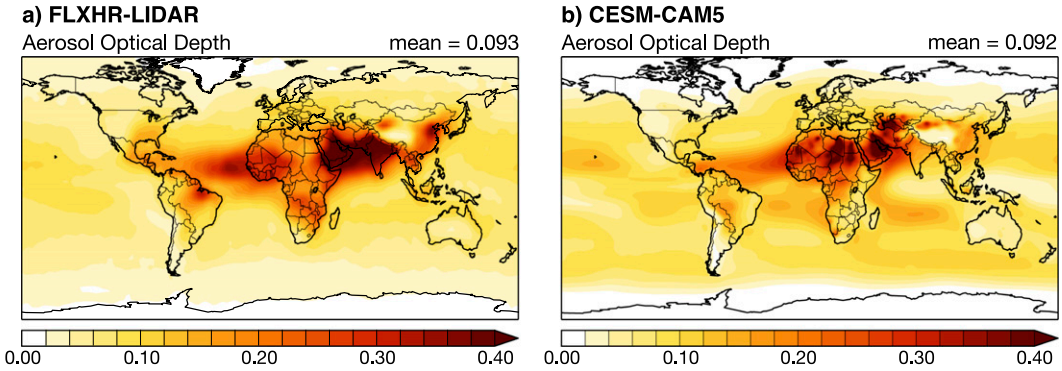


FIG. 2. Maps of annual-mean AOD (a) derived from *CALIPSO* observations and (b) simulated in CESM1(CAM5). Estimates of the global mean are displayed in the top-right corner of each panel.

doubling AOD and systematically attributing all aerosols to smoke cannot account for these differences.

In addition to uncertainties in aerosol properties, discrepancies between observed and simulated DRE over ocean also appear to be linked to the global distribution of clouds. Inconsistencies in the simulated pattern of aerosol direct effects are most evident in high pressure regions over subtropical ocean. Over these regions, CESM1(CAM5) simulates stronger aerosol direct effects than observed in the FLXHR-lidar dataset. Furthermore, the model simulates a lower cloud fraction compared to observations. Since reduced cloudiness over ocean enhances the cooling effect of scattering aerosols, modeled aerosol direct effects are thus strengthened by an underestimate in marine cloud cover.

While clouds are not the only source of DRE biases, cloud cover almost certainly contributes to model biases over some regions. These cloud cover biases in CESM are evident in the global cloudiness statistics. Although CESM1(CAM5) and FLXHR-lidar capture similar

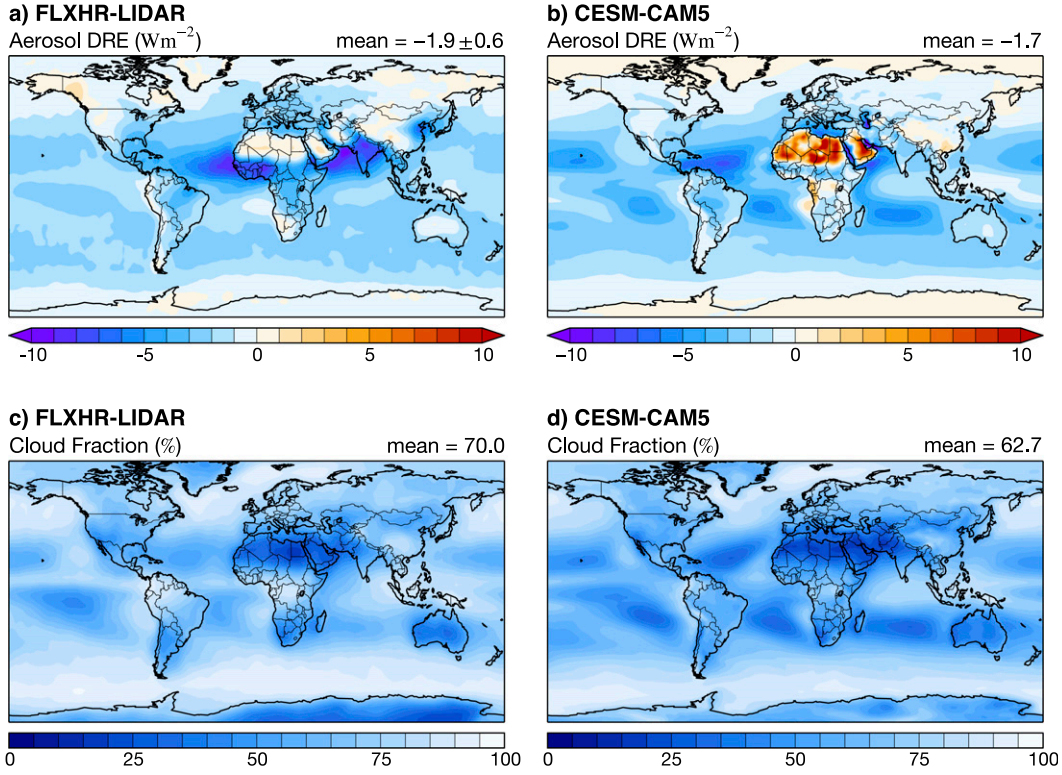


FIG. 3. Annual-mean all-sky DRE and total cloud fraction from (a),(c) FLXHR-lidar and (b),(d) CESM1(CAM5) datasets. Note that whiter regions correspond to higher cloud fraction. Estimates of the global mean are displayed in the top-right corner of each panel.

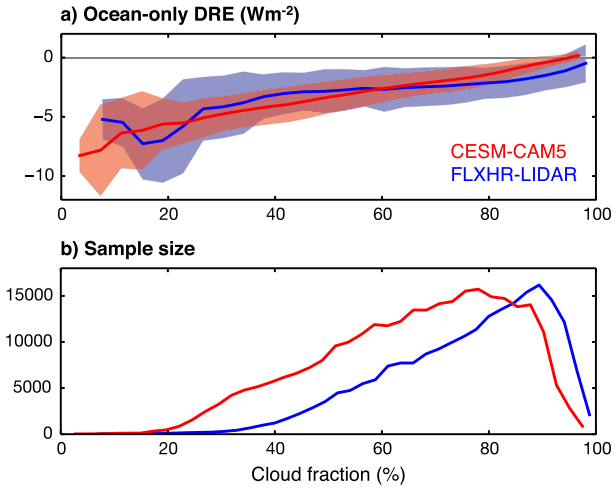


FIG. 4. Observed and modeled PDFs of the (a) all-sky DRE and (b) sample count, over global ocean, expressed as a function of cloud fraction. Monthly averaged estimates of DRE and cloud fraction are evaluated at 2.5° resolution over a 5-yr time period for both FLXHR-lidar (2006–11) and CESM1(CAM5) (2000–05).

large-scale patterns in cloudiness, there are fewer clouds represented in the model. The global-mean cloud fraction is lower in the model (63%) than in observations (70%), which are based on five years of *CloudSat* and *CALIPSO* data. As displayed in Fig. 3, clouds in the subtropics are especially underrepresented in the CESM simulation. In particular, CESM1(CAM5) greatly underestimates the geographical extent of marine stratocumulus clouds in the southeastern Pacific and southeastern Atlantic compared to satellite observations (Kay et al. 2012). Given the strong radiative effects of marine stratocumulus, which cover about 20% of the globe and have a higher albedo compared to ocean, model biases in marine cloud cover likely affect regional estimates of aerosol radiative forcing (Albrecht 1989; Warren et al. 2007).

Qualitatively, Fig. 3 suggests that aerosol direct effects are sensitive to cloud cover. Especially over ocean, stronger DRE coincide with low cloud fraction and weaker DRE coincide with high cloud fraction. In an effort to quantify this effect, Fig. 4a expresses the relationship between DRE and cloud fraction over global ocean. All estimates of DRE and cloud fraction are monthly averaged and evaluated at a 2.5° resolution. The trend of weaker DRE with increasing cloud fraction is consistent in both FLXHR-lidar and CESM1(CAM5). Both datasets show a similar sensitivity of DRE to cloudiness based on the slope of these lines. However, Fig. 4b indicates that CESM1(CAM5) samples about 10% fewer clouds over global ocean than *CloudSat*/*CALIPSO* observations. In other words, the model is skewed more toward clear-sky values, which results in stronger negative DRE over ocean. These findings are consistent with Fig. 3 and suggest that model biases in DRE over ocean are driven primarily by errors in cloud cover as opposed to errors in aerosol properties.

## 4. Regional evidence of the importance of cloud cover

The role of cloud cover in modifying large-scale aerosol radiative effects has received much less attention in the literature than the alternate problem of aerosols modifying cloud radiative effects. Yet a growing body of evidence suggests that global models exhibit large errors in cloud cover over several regions (Bony et al. 2006; Jiang et al. 2012; Kay et al. 2012; Su et al. 2013) and recent studies demonstrate that clouds may have a profound influence on aerosol direct effects (Chung et al. 2005; Chand et al. 2009; Winker et al. 2010). With new vertical structure information provided by active sensors in the A-Train, it is important to revisit this topic to document the potential effects of model cloud biases on simulations of aerosol radiative effects. To investigate these effects, CESM-simulated DRE is evaluated over the southeastern Pacific and southeastern Atlantic. These regions feature semipermanent marine stratocumulus clouds that are known to exert significant influence on the physics and dynamics of the climate system (Teixeira et al. 2011). The sources of aerosols vary greatly over these regions, allowing the effects of cloud cover on scattering and absorbing aerosols to be contrasted.

### *a. Scattering aerosols in the southeastern Pacific*

The southeastern Pacific is known for its wide variability in boundary layer, cloud, and aerosol properties. The region bounded by 35°–5°S, 130°–65°W is adopted to include the full extent of marine stratocumulus clouds along the western coast of South America. The southeastern Pacific is a relatively clean marine environment characterized by contributions from both natural and anthropogenic aerosols, although anthropogenic aerosols predominate near the coast. Clean marine aerosols, consisting of complex mixtures of constituents from various origins, are composed primarily of sea salt and sulfate particles (Blot et al. 2013). This is consistent with *CALIPSO* observations from Fig. 5 that show a dominant aerosol type of "clean marine" consisting of a mixture of sea salt and sulfate. Both sea salt aerosols, produced from the evaporation of sea spray, and sulfate aerosols, produced from the ocean release of dimethylsulfide (DMS), scatter solar radiation and exert a net cooling effect on climate (see Table 1).

Figure 6 compares the spatial distribution of annual-mean DRE and low cloud fraction from the FLXHR-lidar and CESM1(CAM5) datasets. In this study,

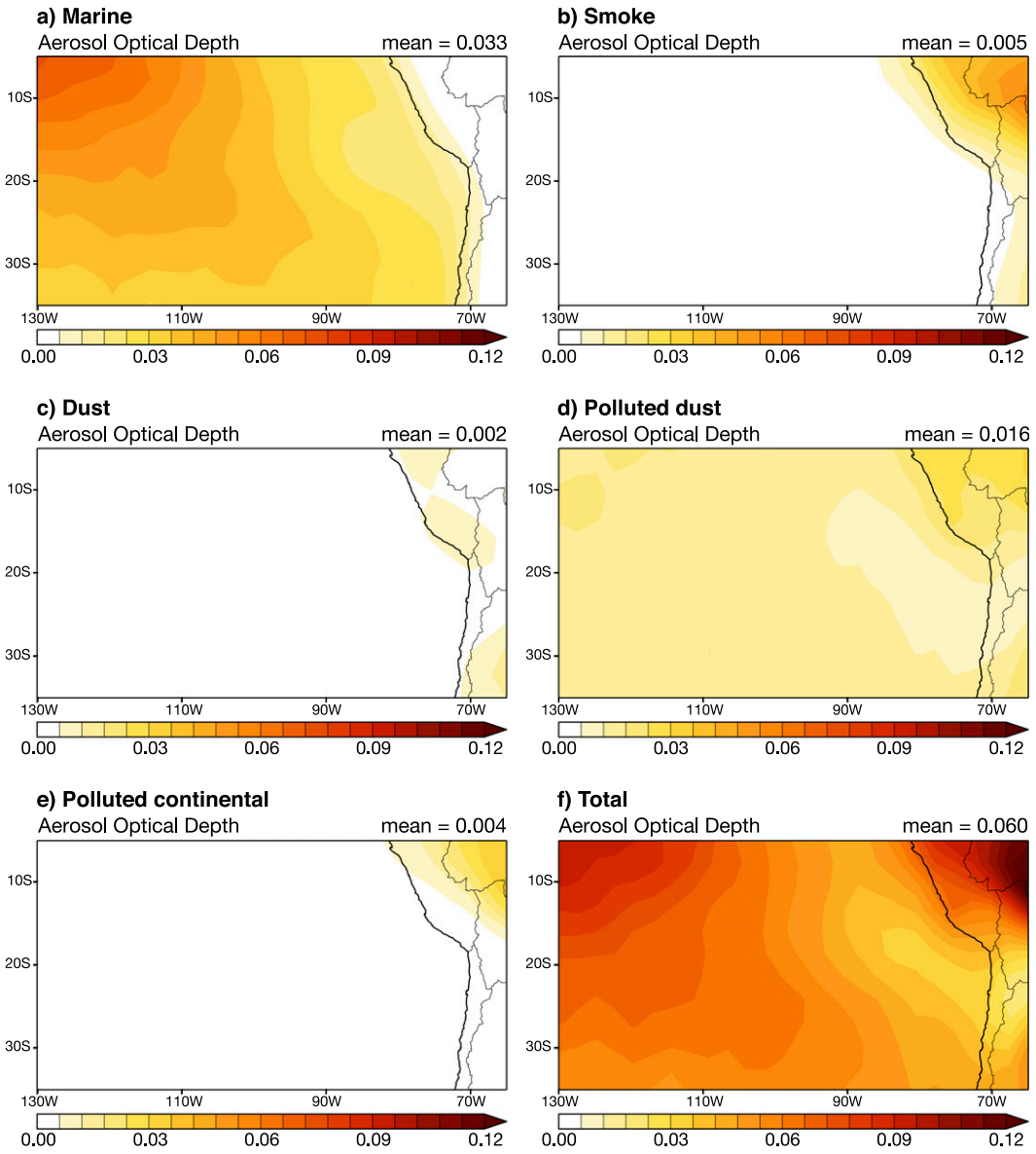


FIG. 5. Maps of annual-mean AOD over the southeastern Pacific (35°–5°S, 130°–65°W) as partitioned by *CALIPSO* aerosol classification types. Estimates of the regional mean are displayed in the top-right corner of each panel.

observed low clouds are identified as those with a cloud-top temperature warmer than 273 K. Figure 6c shows that observed low clouds from *CloudSat*/*CALIPSO* cover an extensive area over the southeastern Pacific. The effect of cloud masking results in weakened aerosol direct radiative effects over ocean (Soden et al. 2004). Consequently, the observed aerosol direct effects are relatively weak and spatially uniform over the ocean, with a regional estimate of $-1.9 \pm 0.6\,\mathrm{W\,m^{-2}}$. In contrast to observations, CESM1(CAM5) simulates a regional estimate of $-2.5\,\mathrm{W\,m^{-2}}$ as illustrated in Fig. 6b. CESM-simulated estimates of DRE exceed $-5\,\mathrm{W\,m^{-2}}$ over an isolated area off the coast of Peru. While uncertainties in aerosol source strength cannot be ruled out, deficiencies in the spatial pattern of clouds almost certainly contribute to the excess model DRE over this region.

Cloud cover influences aerosol radiative effects by modifying the albedo of the underlying surface. As shown in Fig. 6, CESM simulates the strongest aerosol direct effects over areas with the least cloud cover. While the cooling effect of scattering aerosols over the dark ocean can be significant in clear skies, an increase in cloudiness reduces this cooling effect by providing a much brighter background and masking aerosol layers

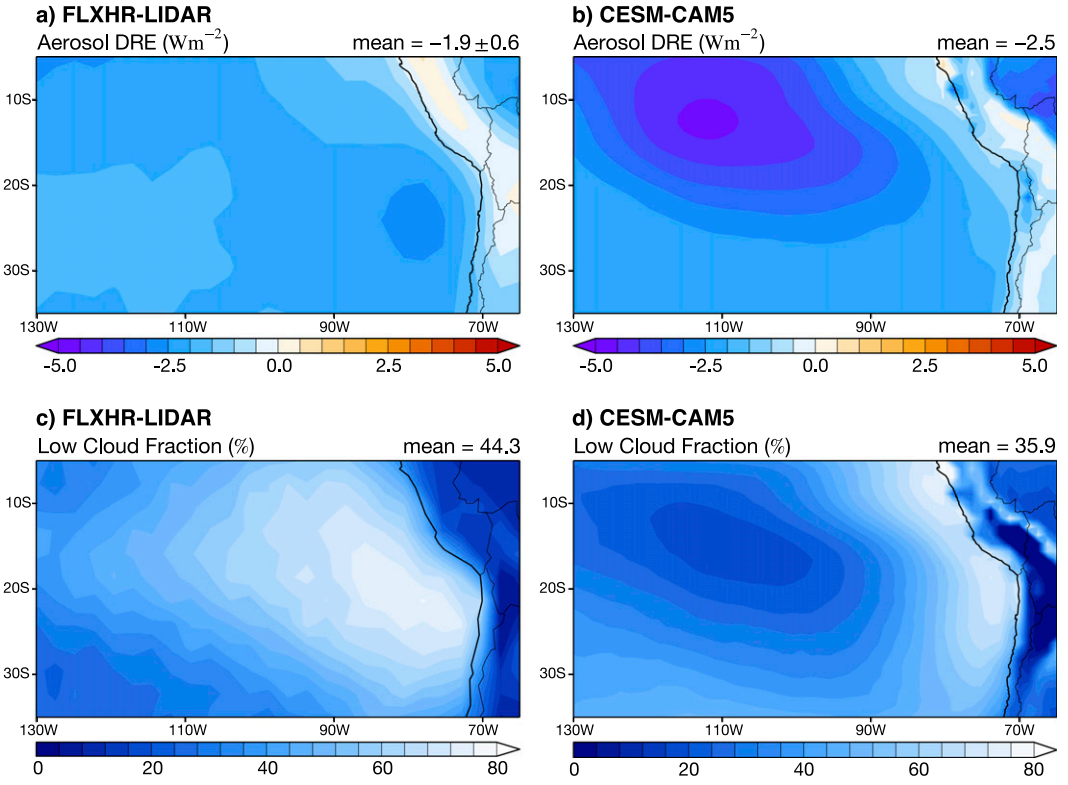


FIG. 6. Annual-mean DRE and low cloud fraction over the southeastern Pacific (35°–5°S, 130°–65°W) from (a),(c) FLXHR-lidar and (b),(d) CESM1(CAM5) datasets. Note that whiter regions correspond to higher cloud fraction. Low clouds are defined on the basis of cloud-top temperatures above 0°C. Estimates of the regional mean are displayed in the top-right corner of each panel.

beneath cloud cover. Overall, CESM1(CAM5) simulates less cloud cover over the southeastern Pacific than observed by *CloudSat* and *CALIPSO*. Figure 6 shows that the meridional extent of low clouds off the coast of Peru is approximately 3 times greater in satellite observations (~3000 km) than the CESM simulation (~1000 km). Furthermore, the simulated low cloud fraction is consistently lower in CESM1(CAM5) (35.9%) than in FLXHR-lidar observations (44.3%). This result is consistent with findings from Kay et al. (2012), who found that CAM5 simulations underestimate the cloud fraction of marine stratocumulus. This reduction in marine stratocumulus cloud cover enhances the cooling effect exerted by scattering marine aerosols, thereby intensifying simulated aerosol radiative effects.

The effect of cloud cover on aerosol radiative effects is further highlighted in the domain-averaged estimates of DRE. As summarized in Table 3, the total aerosol direct effect from FLXHR-lidar observations is $-1.9\,\mathrm{W\,m^{-2}}$. Consistent with Fig. 6, the radiative effects of aerosols are largely buffered by the presence of an extensive marine stratocumulus deck. Accordingly, observed estimates of clear-sky DRE ($-2.1\,\mathrm{W\,m^{-2}}$) and cloudy-sky DRE ($-1.8\,\mathrm{W\,m^{-2}}$) are comparable. Clouds predominate in the southeastern Pacific as 60% of profiles in this region are cloudy sky and the remaining 40% are clear sky. Cloud cover in the southeastern Pacific serves to diminish the cooling effect of scattering aerosols, as reflected in these estimates.

In comparison, the model estimate of the total aerosol direct effect ($-2.5\,\mathrm{W\,m^{-2}}$) is over 30% stronger than observations. This value is influenced by contributions from the simulated clear-sky DRE, which is nearly twice as strong as the observed clear-sky DRE. Furthermore, there is 10% more clear sky simulated in the model than

TABLE 3. Annual-mean DRE ($\mathrm{W\,m^{-2}}$) over the southeastern Pacific (35°–5°S, 130°–65°W) from FLXHR-lidar and CESM1(CAM5) datasets. The fractional occurrence for each category is shown in parentheses. Estimates of the regional mean are displayed in the upper right corner of each map.

| Dataset | Surface | Clear sky | Cloudy sky | All sky |
|---|---|---|---|---|
| FLXHR-lidar | Land | −1.4 (6) | +0.2 (8) | −0.5 (14) |
| | Ocean | −2.1 (34) | −2.1 (52) | −2.1 (86) |
| | Total | −2.1 (40) | −1.8 (60) | −1.9 (100) |
| CESM1(CAM5) | Land | −2.4 (7) | −0.2 (7) | −1.1 (14) |
| | Ocean | −4.0 (38) | −1.8 (48) | −2.8 (86) |
| | Total | −3.8 (45) | −1.6 (55) | −2.5 (100) |

observed by *CloudSat* and *CALIPSO*. While both datasets show good agreement in estimates of cloudy-sky DRE, large discrepancies exist in estimates of clear-sky DRE. The spatial coverage of marine stratocumulus in the southeastern Pacific, therefore, strongly influences the net radiative effect of scattering aerosols.

Overall, the southeastern Pacific provides a perfect natural laboratory to investigate the role of cloud cover on aerosol radiative effects. While the predominantly scattering marine aerosols exert a net cooling effect over this region, the magnitude of this cooling effect is ultimately influenced by cloud cover. Marine stratocumulus clouds exert a strong influence in shaping the regional pattern of aerosol direct effects. While satellite observations identify an expansive cloud deck in the southeastern Pacific, CESM1(CAM5) simulates a cloud deck that is more spatially confined to the coast. Consequently, the CESM1(CAM5) overestimation of aerosol radiative effects in this region likely results from model biases in cloud cover.

### b. *Biomass burning in the southeastern Atlantic*

The southeastern Atlantic features a greater diversity in aerosol sources than the southeastern Pacific. The present study defines the southeastern Atlantic as the region bounded by 25°S–0°, 10°W–30°E and includes the full extent of marine stratocumulus clouds along the western coast of Africa. Biomass burning, a major source of aerosols in southern Africa, is most active during the dry season lasting from July through October (Sakaeda et al. 2011). Over 70% of fires in African savannas are anthropogenic and largely initiated for land clearing and land use change (Sheuyange et al. 2005). In addition to smoke from biomass burning, polluted dust (an external mixture of dust and smoke) is another source of absorbing aerosols over the southeastern Atlantic. Based on *CALIPSO* observations in Fig. 7, smoke and polluted dust are the two aerosol types that contribute the most to total AOD in the southeastern Atlantic. Unlike marine aerosols, however, smoke and polluted dust absorb solar radiation (see Table 1). Given the presence of a semipermanent marine stratocumulus cloud deck over the southeastern Atlantic, aerosol direct effects are therefore sensitive to the relative positions of aerosols and clouds.

Figure 8 compares patterns of annual and seasonal-mean DRE over the southeastern Atlantic from FLXHR-lidar observations and CESM simulation. The total aerosol direct effect averaged over the region is negative, indicative of a net cooling effect, although aerosols exert a localized warming effect off the coast of Angola. This region of positive DRE is consistent with the fact that elevated aerosols layers, advected by the mean flow, can be found at distances greater than 2000 km from the coast (Anderson et al. 2005). The positive aerosol direct effects off the coast of Angola result from absorbing aerosol layers residing above bright clouds (Chand et al. 2009). While all aerosols exert a cooling effect over cloud-free ocean, only absorbing aerosols overlying clouds may exert a warming effect over ocean. Because of the presence of elevated absorbing aerosol layers and low-level clouds, the southeastern Atlantic is a region that frequently exhibits positive aerosol direct effects.

The columns of Fig. 8 illustrate the spatial patterns of observed DRE averaged over December–February (DJF), March–May (MAM), June–August (JJA), and September–November (SON). Since biomass burning in Africa is largely driven by the seasonal migration of the ITCZ, the magnitude of aerosol direct effects in the southeastern Atlantic varies by season. In DJF the observed aerosol direct effect over the southeastern Atlantic is $-2.1\,\mathrm{W\,m^{-2}}$ with an uncertainty of $\pm 0.9\,\mathrm{W\,m^{-2}}$. During this time, biomass burning is largely confined to northern Africa, while southern Africa experiences its rainy season. Consequently, there is limited production of smoke aerosols from December through May. As biomass burning intensifies during JJA, aerosols exert a stronger cooling effect over central Africa and a warming effect off the coast of Angola. Despite increased localized variability, the regional aerosol direct effect in JJA remains negative ($-2.1\,\mathrm{W\,m^{-2}}$). Aerosols exert the strongest warming effect over ocean during SON, with DRE values exceeding $+4\,\mathrm{W\,m^{-2}}$. The location where aerosols exert a warming effect over ocean coincides with the location of marine stratocumulus clouds. Since the warming effects largely offset the cooling effects, the observed DRE of $-0.2\,\mathrm{W\,m^{-2}}$ in SON is significantly weaker than in other seasons. However, greater emissions of absorbing aerosols during SON contribute to a relatively higher uncertainty in the observed DRE ($\pm 1.4\,\mathrm{W\,m^{-2}}$).

CESM1(CAM5) performs well in capturing the large-scale feature of aerosol heating off the coast of Angola. Estimates of annual-mean DRE over the southeastern Atlantic compare favorably between FLXHR-lidar ($-1.7\,\mathrm{W\,m^{-2}}$) and CESM1(CAM5) ($-1.5\,\mathrm{W\,m^{-2}}$). Despite this agreement in the annual mean, observations and simulations disagree on the spatial variability and seasonality of aerosol direct effects. Figure 8 shows that the model simulates an earlier onset of positive DRE off the coast of Angola. While it is more difficult to separate the relative contributions of uncertainties in aerosol properties from those due to differences in cloud cover, it is clear that the model representation of marine stratocumulus in the southeastern Atlantic is more spatially confined to the coast. This almost certainly contributes to aerosol

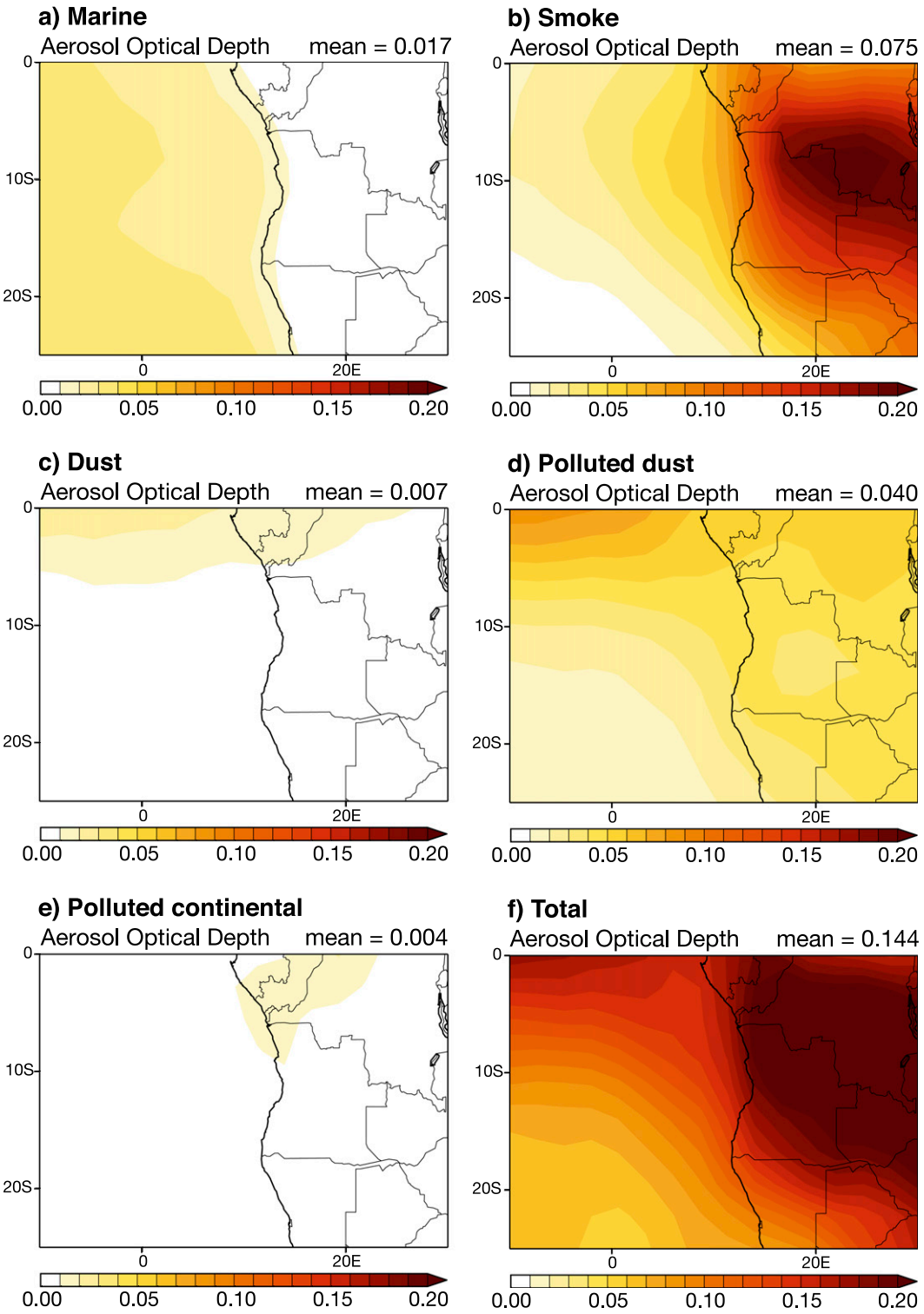


FIG. 7. Maps of annual-mean AOD over the southeastern Atlantic (25°S–0°, 10°W–30°E) as partitioned by *CALIPSO* aerosol classification types. Estimates of the regional mean are displayed in the top-right corner of each panel.

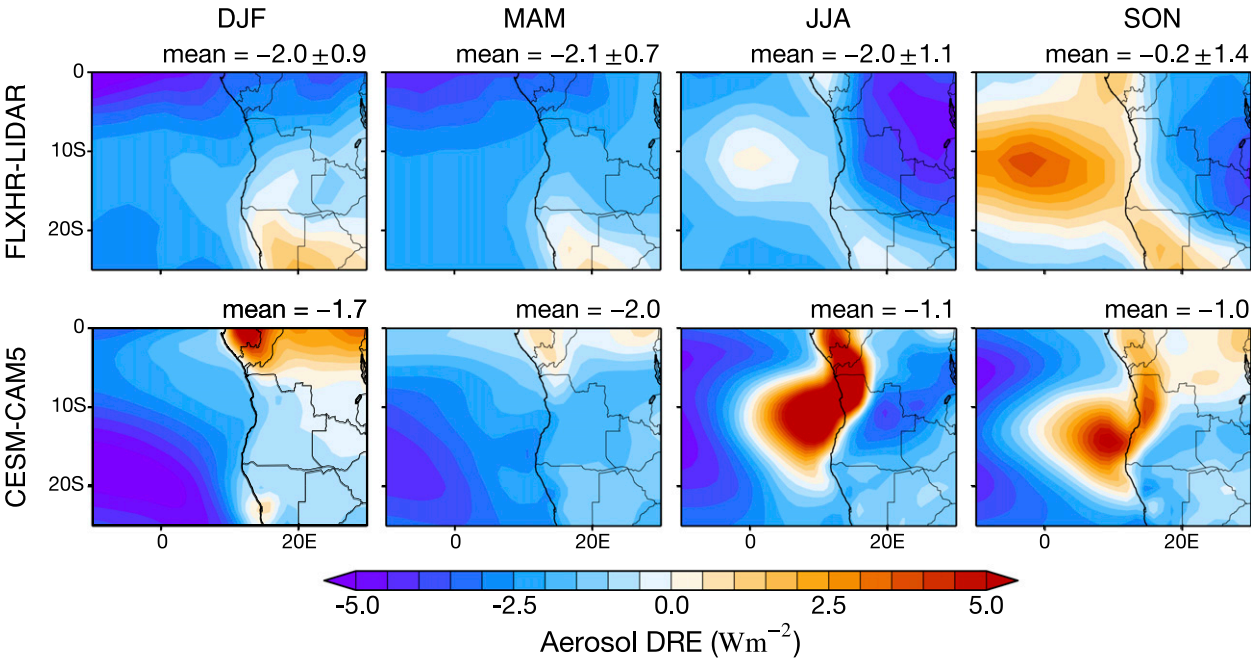


FIG. 8. Seasonally averaged DRE over the southeastern Atlantic (25°S–0°, 10°W–30°E) from (top) FLXHR-lidar and (bottom) CESM1(CAM5) datasets. Estimates of the regional mean are displayed in the top-right corner of each panel.

direct effects that are more spatially confined to the coast. Moreover, the warming effect of aerosols is considerably stronger in the model than observations.

To further illustrate the role clouds play in modulating aerosol direct effects, Fig. 9 displays cumulative density functions of observed seasonally averaged DRE, as partitioned by sky conditions. The results illustrate that aerosol direct effects exhibit a seasonal cycle exclusively in cloudy skies. This seasonal cycle in DRE is more pronounced in the presence of thick clouds than thin clouds. Absorbing aerosols over optically thick clouds exert the strongest warming effect during SON, with 10% of observed DRE estimates larger than $+10\,\mathrm{W\,m^{-2}}$. The cloudy-sky DRE is 5 times more likely to be positive in SON than MAM. There is also greater variability in the range of cloudy-sky DRE observed during SON. This is consistent with Fig. 8, which also shows the greatest spatial variability in aerosol direct effects in SON. Since low-level clouds intensify the warming effect of absorbing aerosols, changes in the distribution of marine stratocumulus clouds can change the sign of DRE from negative to positive (Chand et al. 2009). Consequently, estimates of aerosol direct effects over the southeastern Atlantic are highly sensitive to the relative positions of absorbing aerosols and marine stratocumulus clouds.

Given that marine stratocumulus clouds significantly influence the strength of aerosol direct effects in the southeastern Atlantic, it is worthwhile to compare the observed and modeled seasonal cycles of DRE and the cloud fraction of low clouds (cloud tops warmer than 273 K). Figure 10 plots a time series of the monthly-mean DRE, low cloud fraction, and AOD over the southeastern Atlantic. Both datasets report comparable estimates of the annual-mean DRE with monthly-mean values ranging between $-3$ and $+1\,\mathrm{W\,m^{-2}}$. While both datasets show a seasonal cycle in the total aerosol direct effect, observations and simulations disagree on the timing of this cycle. The observed DRE peaks in September, whereas CESM-simulated DRE peaks one month earlier in August. Cloud cover likely contributes to this timing of the seasonal cycle in DRE. Figure 10 shows that DRE becomes more positive as low cloud fraction increases during JJA at the onset of the biomass burning season. This result is consistent with Chand et al. (2009), who found that the warming effect exerted by absorbing aerosols increases as cloud fraction increases. During JJA, low cloud fraction is consistently higher in CESM1(CAM5) simulation than *CloudSat*/*CALIPSO* observations. Accordingly, simulated aerosol direct effects are more positive in the model during this time period. While these differences in DRE may be attributed to many factors (e.g., aerosol optical depth, aerosol layer height, and aerosol optical properties), cloud cover appears to play a significant role in modulating DRE over subtropical ocean.

The observed and simulated estimates of the annual-mean DRE over the southeastern Atlantic are summarized in Table 4. In the FLXHR-lidar observations, the regional estimate of the total aerosol direct

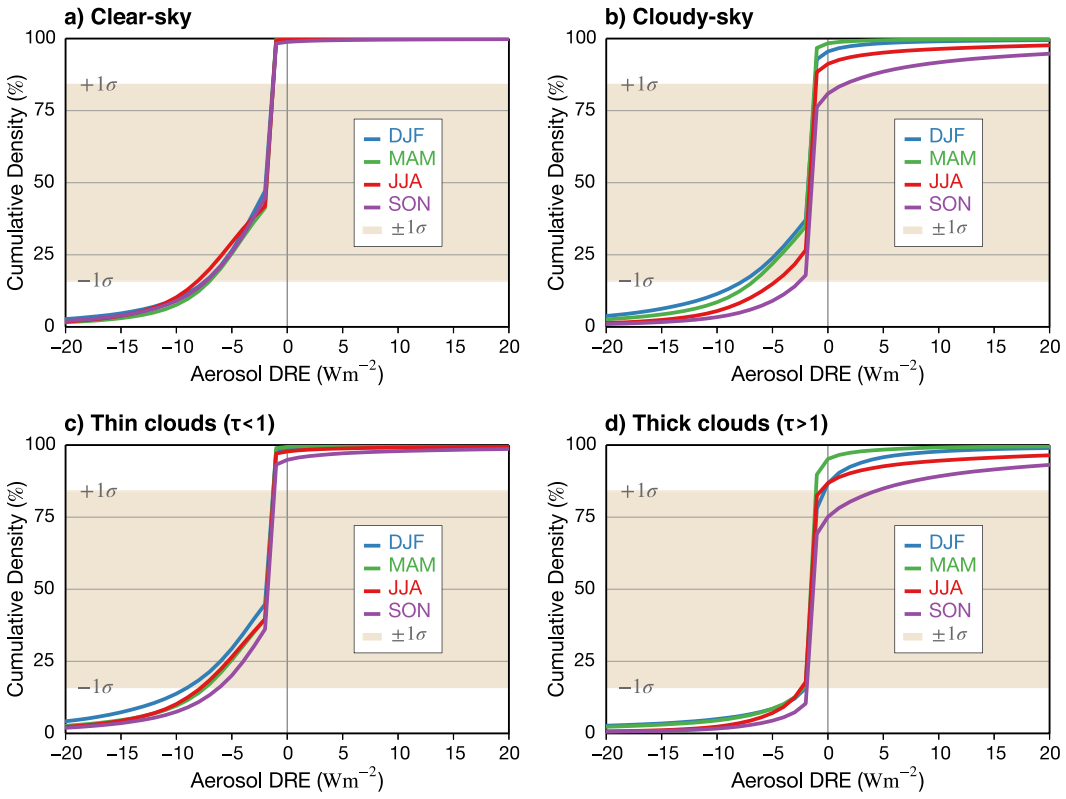


FIG. 9. Cumulative density functions of seasonal-mean DRE over ocean in the southeastern Atlantic (25°S–0°, 10°W–30°E) as sorted by sky conditions from the FLXHR-lidar dataset. The beige shading highlights the spread of data within one standard deviation of the median.

effect is $-1.7\,\mathrm{W\,m^{-2}}$. The cloudy-sky DRE ($-0.6\,\mathrm{W\,m^{-2}}$) is 5 times weaker than the clear-sky DRE ($-3.1\,\mathrm{W\,m^{-2}}$) because of the warming effect exerted by absorbing aerosols over clouds. Despite good agreement between the datasets in the all-sky DRE estimates, cloudy-sky DRE is negative in observations and positive in the model. Compared to FLXHR-lidar observations, CESM1(CAM5) overestimates the warming effect from aerosols. Shindell et al. (2013) found that CAM5 tends to underestimate emissions of biomass burning aerosols over southern Africa. This suggests that marine cloud cover strongly influences the radiative effects of absorbing aerosols. Since aerosol radiative effects depend on both aerosol type and albedo of the underlying surface, discrepancies between observed and simulated DRE are likely explained in part by differences in low-level cloud cover.

In summary, the two main ingredients for positive DRE over ocean—absorbing aerosols and underlying clouds—must both be present for aerosols to exert a warming effect on climate. The southeastern Atlantic is a unique location in that absorbing biomass burning aerosols often reside above bright marine stratocumulus clouds. The resulting warming effect serves to offset the cooling effect of aerosols over the comparatively darker ocean. However, the magnitude and sign of aerosol direct effects are highly sensitive to the precise relative location of aerosols and clouds. Because of unresolved biases in the model treatment of marine stratocumulus clouds and possibly the amount of biomass burning aerosols, there are uncertainties in modeled aerosol direct effects in the southeastern Atlantic. The ability to accurately simulate DRE over this region therefore requires a more realistic representation of the spatial and temporal variability of clouds in addition to improved representation of aerosol sources and optical properties.

## 5. Conclusions

It is well documented that the radiative effects of aerosols contribute to uncertainty in future climate predictions. Global assessments of aerosol direct effects remain challenging because of incomplete knowledge of aerosol characteristics on large space and time scales, especially in the presence of clouds and above bright surfaces. While the effects of aerosols on cloud radiative forcing have been extensively studied, the effects of clouds on aerosol radiative forcing have received much

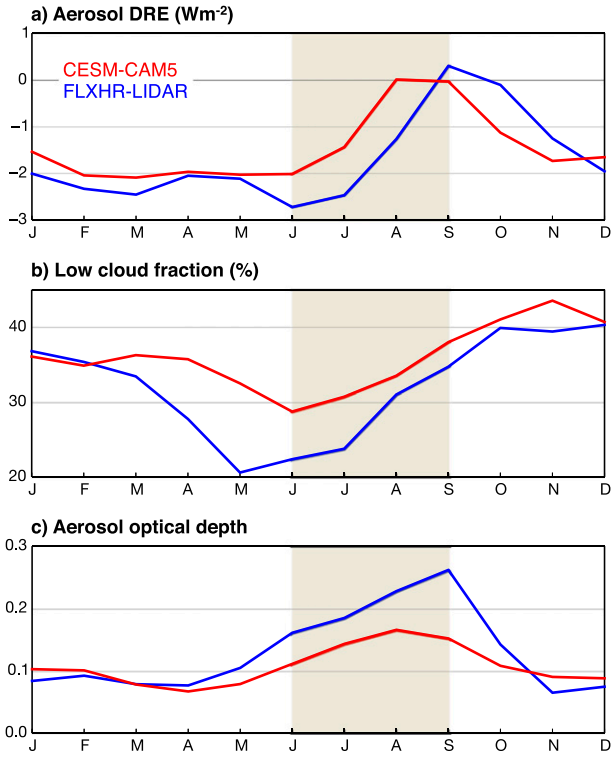


FIG. 10. Monthly-mean estimates of (a) DRE, (b) low cloud fraction, and (c) AOD over the southeastern Atlantic (25°S–0°, 10°W–30°E) from FLXHR-lidar and CESM1(CAM5) datasets. For reference, the JJA season is highlighted to draw attention to the onset of the biomass burning season.

less attention, particularly on global scales, as a result of a lack of suitable observations.

While not immune to uncertainties, new multisensor observations from the A-Train satellite constellation provide key observational constraints necessary to identify and reduce uncertainties in model simulations of aerosol direct effects, especially those resulting from biases in the spatial and temporal distributions of clouds. *CloudSat*'s new multisensor radiative fluxes and heating rates product leverages high-quality vertically resolved cloud and aerosol measurements critical to fill in the gaps in our understanding of aerosol radiative effects. Using this dataset, the present study seeks to improve upon previous efforts to assess the representation of aerosol direct effects in models by providing observational estimates of aerosol direct effects in both clear and cloudy skies. The results provide guidance for evaluating the impact of model cloud biases on simulated aerosol direct effects.

The global annual-mean DRE estimated from the FLXHR-lidar dataset is $-1.9\,\mathrm{W\,m^{-2}}$, a value that is in better agreement with estimates from global models than previous satellite-based techniques. Uncertainty in this global-mean value is $\pm 0.6\,\mathrm{W\,m^{-2}}$, owing primarily to misclassification of aerosol types (Omar et al. 2013) and uncertainty in aerosol optical properties. The results may also be subject to underestimation of thin aerosol layers, especially in the presence of clouds (Kacenelenbogen et al. 2014), and misclassification of dense aerosol layers as clouds (Schuster et al. 2012). These uncertainties may partially offset one another but are difficult to quantify given current satellite instrumentation. The combination of simultaneous backscatter and extinction measurements from multiwavelength High Spectral Resolution Lidar (HSRL) and phase function information from polarimeters being developed for the next generation of atmospheric composition satellites offers the potential to significantly reduce many of these sources of uncertainty in the near future.

While CESM1(CAM5) captures many large-scale features in observed aerosol direct effects, several large regional discrepancies exist that appear to be at least partially linked to biases in model cloud cover. An underrepresentation of low-level clouds in the southeastern Pacific, for example, leads to overestimates of the cooling effects of scattering aerosols. Likewise, a poor representation of the seasonal cycle of cloudiness in the southeastern Atlantic causes the model to overestimate the warming effects of absorbing aerosols early in the biomass burning season. These case studies highlight the important role clouds play in modulating aerosol direct effects. While a number of studies have documented the need for improving aerosol sources and optical properties in global models, the impact of cloud biases on aerosol

TABLE 4. Annual-mean DRE ($\mathrm{W\,m^{-2}}$) over the southeastern Atlantic (25°S–0°, 10°W–30°E) from FLXHR-lidar and CESM1(CAM5) datasets. The fractional occurrence for each category is shown in parentheses. The values of $\sigma$ represent the standard deviations of 2.5° DRE estimates within the region.

| | | Clear sky | | Cloudy sky | | All sky | |
|---|---|---|---|---|---|---|---|
| Dataset | Surface | Mean | $\sigma$ | Mean | $\sigma$ | Mean | $\sigma$ |
| FLXHR-lidar | Land | −3.2 (18) | 2.5 | −1.1 (19) | 1.7 | −2.0 (37) | 1.6 |
| | Ocean | −2.9 (17) | 0.9 | −0.3 (46) | 1.0 | −1.4 (63) | 1.0 |
| | Total | −3.1 (35) | 1.9 | −0.6 (65) | 1.4 | −1.7 (100) | 1.4 |
| CESM1(CAM5) | Land | −3.5 (18) | 1.4 | +1.2 (19) | 1.9 | −0.7 (37) | 1.3 |
| | Ocean | −5.8 (27) | 0.6 | +0.5 (36) | 1.9 | −2.2 (63) | 1.6 |
| | Total | −4.9 (45) | 1.5 | +0.9 (55) | 2.0 | −1.5 (100) | 1.7 |

direct radiative effects has not been as widely discussed. Given known uncertainties in model cloud cover and feedbacks, the results presented here suggest that the influence of clouds on aerosol radiative effects may represent an important source of uncertainty in regional climate predictions.

*Acknowledgments.* This research was supported by NASA CloudSat Mission Grant NNX12AC51G. All *CloudSat* data presented here were acquired through the DPC and at the time of writing can be accessed online at http://www.cloudsat.cira.colostate.edu. The authors thank the staff at the *CloudSat* Data Processing Center (DPC) for their help in data processing. The authors gratefully acknowledge Natalie Mahowald for her helpful insights into the model representation of mineral dust in CESM1(CAM5).

## REFERENCES

Albrecht, B. A., 1989: Aerosols, cloud microphysics, and fractional cloudiness. *Science,* **245,** 1227–1230, doi:10.1126/science.245.4923.1227.

Anderson, T. L., and Coauthors, 2005: An A-Train strategy for quantifying direct climate forcing by anthropogenic aerosols. *Bull. Amer. Meteor. Soc.,* **86,** 1795–1809, doi:10.1175/BAMS-86-12-1795.

Bellouin, N., O. Boucher, J. Haywood, and M. S. Reddy, 2005: Global estimate of aerosol direct radiative forcing from satellite measurements. *Nature,* **438,** 1138–1141, doi:10.1038/nature04348.

Bergamo, A., A. M. Tafuro, S. Kinne, F. De Tomasi, and M. R. Perrone, 2008: Monthly-averaged anthropogenic aerosol direct radiative forcing over the Mediterranean from AERONET derived aerosol properties. *Atmos. Chem. Phys. Discuss.,* **8,** 12 769–12 822, doi:10.5194/acpd-8-12769-2008.

Blot, R., and Coauthors, 2013: Ultrafine sea spray aerosol over the southeastern Pacific: Open-ocean contributions to marine boundary layer CCN. *Atmos. Chem. Phys.,* **13,** 7263–7278, doi:10.5194/acp-13-7263-2013.

Bony, S., and Coauthors, 2006: How well do we understand and evaluate climate change feedback processes? *J. Climate,* **19,** 3445–3482, doi:10.1175/JCLI3819.1.

Chand, D., R. Wood, T. L. Anderson, S. K. Satheesh, and R. J. Charlson, 2009: Satellite-derived direct radiative effect of aerosols dependent on cloud cover. *Nat. Geosci.,* **2,** 181–184, doi:10.1038/ngeo437.

——, and Coauthors, 2012: Aerosol optical depth increase in partly cloudy conditions. *J. Geophys. Res.,* **117,** D17207, doi:10.1029/2012JD017894.

Chepfer, H., S. Bony, D. Winker, G. Cesana, J. L. Dufresne, P. Minnis, C. J. Stubenrauch, and S. Zeng, 2010: The GCM-oriented *CALIPSO* cloud product (*CALIPSO*-GOCCP). *J. Geophys. Res.,* **115,** D00H16, doi:10.1029/2009JD012251.

Chin, M., R. A. Kahn, and S. E. Schwartz, 2009: *Atmospheric Aerosol Properties and Climate Impacts*. DIANE Publishing, 115 pp.

Chung, C. E., V. Ramanathan, D. Kim, and I. A. Podgorny, 2005: Global anthropogenic aerosol direct forcing derived from satellite and ground-based observations. *J. Geophys. Res.,* **110,** D24207, doi:10.1029/2005JD006356.

de Graaf, M., L. G. Tilstra, P. Wang, and P. Stammes, 2012: Retrieval of the aerosol direct radiative effect over clouds from spaceborne spectrometry. *J. Geophys. Res. Atmos.,* **117,** D07207, doi:10.1029/2011JD017160.

Di Biagio, C., A. di Sarra, and D. Meloni, 2010: Large atmospheric shortwave radiative forcing by Mediterranean aerosols derived from simultaneous ground-based and spaceborne observations and dependence on the aerosol type and single scattering albedo. *J. Geophys. Res.,* **115,** D10209, doi:10.1029/2009JD012697.

Fu, Q., and K. N. Liou, 1992: On the correlated *k*-distribution method for radiative transfer in nonhomogeneous atmospheres. *J. Atmos. Sci.,* **49,** 2139–2156, doi:10.1175/1520-0469(1992)049<2139:OTCDMF>2.0.CO;2.

Hansen, J., M. Sato, and R. Ruedy, 1997: Radiative forcing and climate response. *J. Geophys. Res.,* **102** (D6), 6831–6864, doi:10.1029/96JD03436.

Haywood, J. M., 2003: The mean physical and optical properties of regional haze dominated by biomass burning aerosol measured from the C-130 aircraft during SAFARI 2000. *J. Geophys. Res.,* **108,** 8473, doi:10.1029/2002JD002226.

Henderson, D. S., and T. S. L'Ecuyer, 2011: Level 2B fluxes and heating rates and 2B fluxes and heating rates with lidar process description and interface control document. JPL Tech. Doc., NASA, 28 pp. [Available online at http://www.cloudsat.cira.colostate.edu/sites/default/files/products/files/2B-FLXHR-LIDAR_PDICD.P2_R04.20111220.pdf.]

——, ——, G. Stephens, P. Partain, and M. Sekiguchi, 2013: A multisensor perspective on the radiative impacts of clouds and aerosols. *J. Appl. Meteor. Climatol.,* **52,** 853–871, doi:10.1175/JAMC-D-12-025.1.

Hurrell, J. W., and Coauthors, 2013: The Community Earth System Model: A framework for collaborative research. *Bull. Amer. Meteor. Soc.,* **94,** 1339–1360, doi:10.1175/BAMS-D-12-00121.1.

Jaeglé, L., P. K. Quinn, T. S. Bates, B. Alexander, and J.-T. Lin, 2011: Global distribution of sea salt aerosols: New constraints from in situ and remote sensing observations. *Atmos. Chem. Phys.,* **11,** 3137–3157, doi:10.5194/acp-11-3137-2011.

Jiang, J. H., and Coauthors, 2012: Evaluation of cloud and water vapor simulations in CMIP5 climate models using NASA A-Train satellite observations. *J. Geophys. Res.,* **117,** D14105, doi:10.1029/2011JD017237.

Kacenelenbogen, M., and Coauthors, 2014: An evaluation of CALIOP/*CALIPSO*'s aerosol-above-cloud detection and retrieval capability over North America. *J. Geophys. Res. Atmos.,* **119,** 230–244, doi:10.1002/2013JD020178.

Kaufman, Y. J., O. Boucher, D. Tanré, M. Chin, L. A. Remer, and T. Takemura, 2005: Aerosol anthropogenic component estimated from satellite data. *Geophys. Res. Lett.,* **32,** L17804, doi:10.1029/2005GL023125.

Kay, J. E., and Coauthors, 2012: Exposing global cloud biases in the Community Atmosphere Model (CAM) using satellite observations and their corresponding instrument simulators. *J. Climate,* **25,** 5190–5207, doi:10.1175/JCLI-D-11-00469.1.

Kittaka, C., D. M. Winker, M. A. Vaughan, A. Omar, and L. A. Remer, 2011: Intercomparison of column aerosol optical depths from *CALIPSO* and MODIS-*Aqua*. *Atmos. Meas. Tech.,* **4,** 131–141, doi:10.5194/amt-4-131-2011.

Lamarque, J.-F., and Coauthors, 2013: The Atmospheric Chemistry and Climate Model Intercomparison Project (ACCMIP): Overview and description of models, simulations and climate diagnostics. *Geosci. Model Dev.,* **6,** 179–206, doi:10.5194/gmd-6-179-2013.

L'Ecuyer, T. S., and J. Jiang, 2010: Touring the atmosphere aboard the A-Train. *Phys. Today,* **63,** 36, doi:10.1063/1.3463626.

——, N. B. Wood, T. Haladay, G. L. Stephens, and P. W. Stackhouse, 2008: Impact of clouds on atmospheric heating based on the R04 *CloudSat* fluxes and heating rates data set. *J. Geophys. Res.,* **113,** D00A15, doi:10.1029/2008JD009951.

Liu, X., and Coauthors, 2012: Toward a minimal representation of aerosols in climate models: Description and evaluation in the Community Atmosphere Model CAM5. *Geosci. Model Dev.,* **5,** 709–739, doi:10.5194/gmd-5-709-2012.

Loeb, N., and N. Manalo-Smith, 2005: Top-of-atmosphere direct radiative effect of aerosols over global oceans from merged CERES and MODIS observations. *J. Climate,* **18,** 3506–3526, doi:10.1175/JCLI3504.1.

Moody, E. G., M. D. King, S. Member, S. Platnick, and C. B. Schaaf, 2005: Spatially complete global spectral surface albedos: Value-added datasets derived from *Terra* MODIS land products. *IEEE Trans. Geosci. Remote Sens.,* **43,** 144–158, doi:10.1109/TGRS.2004.838359.

Myhre, G., 2009: Consistency between satellite-derived and modeled estimates of the direct aerosol effect. *Science,* **325,** 187–190, doi:10.1126/science.1174461.

——, Y. Govaerts, J. M. Haywood, T. K. Berntsen, and A. Lattanzio, 2005: Radiative effect of surface albedo change from biomass burning. *Geophys. Res. Lett.,* **32,** L20812, doi:10.1029/2005GL022897.

——, and Coauthors, 2007: Comparison of the radiative properties and direct radiative effect of aerosols from a global aerosol model and remote sensing data over ocean. *Tellus,* **59B,** 115–129, doi:10.1111/j.1600-0889.2006.00226.x.

Neale, R., and C. Chen, 2010: Description of the NCAR Community Atmosphere Model (CAM 5.0). NCAR Tech. Note NCAR/TN-486+STR, 274 pp.

Omar, A. H., and Coauthors, 2009: The *CALIPSO* automated aerosol classification and lidar ratio selection algorithm. *J. Atmos. Oceanic Technol.,* **26,** 1994–2014, doi:10.1175/2009JTECHA1231.1.

——, and Coauthors, 2013: CALIOP and AERONET aerosol optical depth comparisons: One size fits none. *J. Geophys. Res. Atmos.,* **118,** 4748–4766, doi:10.1002/jgrd.50330.

Patadia, F., P. Gupta, and S. A. Christopher, 2008: First observational estimates of global clear sky shortwave aerosol direct radiative effect over land. *Geophys. Res. Lett.,* **35,** L04810, doi:10.1029/2007GL032314.

Penner, J. E., 2003: Soot and smoke aerosol may not warm climate. *J. Geophys. Res.,* **108,** 4657, doi:10.1029/2003JD003409.

Quijano, A. L., I. N. Sokolik, and O. B. Toon, 2000: Radiative heating rates and direct radiative forcing by mineral dust in cloudy atmospheric conditions. *J. Geophys. Res.,* **105,** 12 207–12 219, doi:10.1029/2000JD900047.

Redemann, J., M. A. Vaughan, Q. Zhang, Y. Shinozuka, P. B. Russell, J. M. Livingston, M. Kacenelenbogen, and L. A. Remer, 2012: The comparison of MODIS-*Aqua* (C5) and CALIOP (V2 & V3) aerosol optical depth. *Atmos. Chem. Phys.,* **12,** 3025–3043, doi:10.5194/acp-12-3025-2012.

Remer, L. A., and Coauthors, 2005: The MODIS aerosol algorithm, products, and validation. *J. Atmos. Sci.,* **62,** 947–973, doi:10.1175/JAS3385.1.

Ritter, B., and J.-F. Geleyn, 1992: A comprehensive radiation scheme for numerical weather prediction models with potential applications in climate simulations. *Mon. Wea. Rev.,* **120,** 303–325, doi:10.1175/1520-0493(1992)120<0303:ACRSFN>2.0.CO;2.

Sakaeda, N., R. Wood, and P. J. Rasch, 2011: Direct and semidirect aerosol effects of southern African biomass burning aerosol. *J. Geophys. Res.,* **116,** D12205, doi:10.1029/2010JD015540.

Satheesh, S., and K. Krishna Moorthy, 2005: Radiative effects of natural aerosols: A review. *Atmos. Environ.,* **39,** 2089–2110, doi:10.1016/j.atmosenv.2004.12.029.

Schulz, M., and Coauthors, 2006: Radiative forcing by aerosols as derived from the AeroCom present-day and pre-industrial simulations. *Atmos. Chem. Phys.,* **6,** 5225–5246, doi:10.5194/acp-6-5225-2006.

Schuster, G. L., M. Vaughan, D. MacDonnell, W. Su, D. Winker, O. Dubovik, T. Lapyonok, and C. Trepte, 2012: Comparison of *CALIPSO* aerosol optical depth retrievals to AERONET measurements, and a climatology for the lidar ratio of dust. *Atmos. Chem. Phys.,* **12,** 7431–7452, doi:10.5194/acp-12-7431-2012.

Sheuyange, A., G. Oba, and R. B. Weladji, 2005: Effects of anthropogenic fire history on savanna vegetation in northeastern Namibia. *J. Environ. Manage.,* **75,** 189–198, doi:10.1016/j.jenvman.2004.11.004.

Shindell, D. T., and Coauthors, 2013: Radiative forcing in the ACCMIP historical and future climate simulations. *Atmos. Chem. Phys.,* **13,** 2939–2974, doi:10.5194/acp-13-2939-2013.

Soden, B., A. Broccoli, and R. Hemler, 2004: On the use of cloud forcing to estimate cloud feedback. *J. Climate,* **17,** 3661–3665, doi:10.1175/1520-0442(2004)017<3661:OTUOCF>2.0.CO;2.

Su, H., and Coauthors, 2013: Diagnosis of regime-dependent cloud simulation errors in CMIP5 models using ''A-Train'' satellite observations and reanalysis data. *J. Geophys. Res. Atmos.,* **118,** 2762–2780, doi:10.1029/2012JD018575.

Takemura, T., T. Nakajima, O. Dubovik, B. N. Holben, and S. Kinne, 2002: Single-scattering albedo and radiative forcing of various aerosol species with a global three-dimensional model. *J. Climate,* **15,** 333–352, doi:10.1175/1520-0442(2002)015<0333:SSAARF>2.0.CO;2.

Teixeira, J., and Coauthors, 2011: Tropical and subtropical cloud transitions in weather and climate prediction models: The GCSS/WGNE Pacific Cross-Section Intercomparison (GPCI). *J. Climate,* **24,** 5223–5256, doi:10.1175/2011JCLI3672.1.

Torres, O., A. Tanskanen, B. Veihelmann, C. Ahn, R. Braak, P. K. Bhartia, P. Veefkind, and P. Levelt, 2007: Aerosols and surface UV products from Ozone Monitoring Instrument observations: An overview. *J. Geophys. Res.,* **112,** D24S47, doi:10.1029/2007JD008809.

Vaughan, M. A., and Coauthors, 2009: Fully automated detection of cloud and aerosol layers in the *CALIPSO* lidar measurements. *J. Atmos. Oceanic Technol.,* **26,** 2034–2050, doi:10.1175/2009JTECHA1228.1.

Waquet, F., J. Riedi, L. C. Labonnote, P. Goloub, B. Cairns, J.-L. Deuzé, and D. Tanré, 2009: Aerosol remote sensing over clouds using A-Train observations. *J. Atmos. Sci.,* **66,** 2468–2480, doi:10.1175/2009JAS3026.1.

Warren, S. G., R. M. Eastman, and C. J. Hahn, 2007: A survey of changes in cloud cover and cloud types over land from surface observations, 1971–96. *J. Climate,* **20,** 717–738, doi:10.1175/JCLI4031.1.

Wilcox, E., 2012: Direct and semi-direct radiative forcing of smoke aerosols over clouds. *Atmos. Chem. Phys.,* **12,** 139–149, doi:10.5194/acp-12-139-2012.

Winker, D. M., and Coauthors, 2010: The CALIPSO Mission: A global 3D view of aerosols and clouds. *Bull. Amer. Meteor. Soc.,* **91,** 1211–1229, doi:10.1175/2010BAMS3009.1.

Worley, P., and A. Craig, 2012: Performance of the Community Earth System Model. *Int. J. High Perform. Comput. Appl.,* **26,** 17–30.

Yu, H., and Coauthors, 2006: A review of measurement-based assessments of the aerosol direct radiative effect and forcing. *Atmos. Chem. Phys.,* **6,** 613–666, doi:10.5194/acp-6-613-2006.